

# Infrared photometry of the dwarf nova V2051 Ophiuchi: II - The quiescent accretion disc and its spiral arms <sup>★</sup>

Raymundo Baptista<sup>1</sup> † and Eduardo Wojcikiewicz<sup>1</sup>

<sup>1</sup>*Departamento de Física, Universidade Federal de Santa Catarina, Campus Trindade, 88040-900 Florianópolis, SC, Brazil*

Accepted 2019 December 12. Received 2019 December 3; in original form 2019 October 7

## ABSTRACT

We report the analysis of time-series of infrared  $JHK_s$  photometry of the dwarf nova V2051 Oph in quiescence with eclipse mapping techniques to investigate structures and the spectrum of its accretion disc. The light curves after removal of the ellipsoidal variations caused by the mass-donor star show a double-wave modulation signalling the presence of two asymmetric light sources in the accretion disc. Eclipse maps reveal two spiral arms on top of the disc emission, one at  $R_1 = 0.28 \pm 0.02 R_{L1}$  and the other at  $R_2 = 0.42 \pm 0.02 R_{L1}$  (where  $R_{L1}$  is the distance from disc centre to the inner Lagrangian point), which are seen face-on at binary phases consistent with the maxima of the double-wave modulation. The wide open angle inferred for the spiral arms ( $\theta_s = 21^\circ \pm 4^\circ$ ) suggests the quiescent accretion disc of V2051 Oph has high viscosity. The accretion disc is hot and optically thin in its inner regions ( $T_{\text{gas}} \sim 10 - 12 \times 10^3 \text{ K}$  and surface densities  $\sim 10^{-3} - 10^{-2} \text{ g cm}^{-2}$ ), and becomes cool and opaque in its outer regions.

**Key words:** accretion, accretion discs – binaries: eclipsing – binaries:close – stars: dwarf novae – stars: individual (V2051 Ophiuchi)

## 1 INTRODUCTION

Dwarf novae are short period interacting binaries where a late type star overfills its Roche lobe and transfers matter to a companion white dwarf (WD) via an accretion disc. They show days-long outbursts where the disc brightens by 2-5 mag and which recur on timescales of days to weeks. Aside of the normal outbursts, the sub-class of the SU UMa stars show stronger, longer and more regular superoutbursts characterized by the appearance of superhumps, believed to be the result of the tidal interaction of the donor star with a slowly precessing, elliptical outer ring which develops when the disc expands beyond the 3:1 resonance radius (e.g., Whitehurst 1988; Hirose & Osaki 1990; Lubow 1994). Accretion discs in dwarf novae are also prone to the appearance of tidally-induced, wide open spiral density waves if the disc is hot

and/or highly viscous (e.g., Sawada, Matsuda & Hachisu 1986; Steeghs, Harlaftis & Horne 1997; Stehle 1999).

Dwarf nova outbursts are thought to be driven either by bursts of increased mass transfer rate (Mass Transfer Instability Model, MTIM, e.g., Bath & Pringle 1981) or by a thermal-viscous disc instability (Disc Instability Model, DIM, e.g. Lasota 2001). MTIM interprets the outburst as the response of a constant, high viscosity <sup>1</sup> disc ( $\alpha \sim 0.1 - 1$ , from the decline timescale of outbursting dwarf novae, e.g., Warner 1995) to a burst of mass transfer from the donor star. On the other hand, DIM predicts matter accumulates in a cool, low viscosity disc during quiescence ( $T_{\text{ef}} < T_{\text{crit1}} \sim 7000 \text{ K}$ ,  $\alpha_{\text{cool}} \sim 10^{-2}$ ) which switches to a hot, high-viscosity regime during outbursts ( $T_{\text{ef}} > T_{\text{crit2}} \sim 10000 \text{ K}$ ,  $\alpha_{\text{hot}} \simeq 10 \alpha_{\text{cool}} \sim 0.1$ ). This limit-cycle scheme implies that the disc temperatures must be  $T_{\text{ef}} < T_{\text{crit1}}$  in quiescence and  $T_{\text{ef}} > T_{\text{crit2}}$  during outbursts, making the comparison of observed quiescent and outburst disc temperatures with  $T_{\text{crit1}}$  and  $T_{\text{crit2}}$  a key test for DIM.

V2051 Oph is a short-period ( $P_{\text{orb}} = 90 \text{ min}$ ) eclips-

<sup>★</sup> Based on observations obtained at the Southern Astrophysical Research (SOAR) telescope, which is a joint project of the Ministério da Ciência, Tecnologia, Inovações e Comunicações (MCTIC) do Brasil, the U.S. National Optical Astronomy Observatory (NOAO), the University of North Carolina at Chapel Hill (UNC), and Michigan State University (MSU).

† E-mail: raybap@gmail.com (RB)

<sup>1</sup> here we adopt the prescription of Shakura & Sunyaev (1973) for the accretion disc viscosity,  $\nu = \alpha c_s H$ , where  $\alpha$  is the non-dimensional viscosity parameter,  $c_s$  is the local sound speed and  $H$  is the disc scaleheight.

ing dwarf nova showing large-amplitude flickering (random brightness fluctuations of 0.1–1 mag), deep eclipses ( $\Delta M_B \simeq 2.5$  mag) and a plethora of different eclipse profiles (Warner & Cropper 1983; Cook & Brunt 1983; Warner & O’Donoghue 1987). Superoutbursts were observed and superhumps were detected by Kiyota & Kato (1998), Vrielman & Offutt (2003) and Patterson et al. (2003), implying that V2051 Oph is an SU UMa type dwarf nova. Baptista et al. (1998) used HST and ground-based observations to constrain the binary parameters, finding a mass ratio of  $q = 0.19 \pm 0.03$ , an inclination of  $i = 83.3^\circ \pm 1.4^\circ$ , and precise values for the mass and radius of both stars.

The multi-color photometric study of Vrielmann, Stiening & Offutt (2002) and the UV-optical spectroscopic study of Saito & Baptista (2006) both suggest that the quiescent accretion disc of V2051 Oph has a hot, optically thin chromosphere responsible for the emission lines, possibly enveloping a cooler and opaque underlying disc. Papadaki et al. (2008) performed Doppler tomography of V2051 Oph in quiescence, two days after the end of a superoutburst in 1999. Their Balmer and He I tomograms show two asymmetric arcs at opposite sides of the accretion disc, reminiscent of the spiral structures seen in Doppler tomograms of IP Peg in outburst (e.g., Steeghs, Harlaftis & Horne 1997), which they instead associated with the bright spot and with the superhump light source. H I, He I and O I Doppler tomography of V2051 Oph in quiescence several months after its previous outburst also shows two asymmetric arcs extended in azimuth at opposite sides of the accretion disc, which were then interpreted as being tidally-induced spiral arms (Rutkowski et al. 2016).

An eclipse mapping investigation of the flickering sources by Baptista & Bortoletto (2004) reveal that the low-frequency flickering arises mainly in the overflowing/penetrating gas stream, while the high-frequency flickering originates in the accretion disc, suggesting a quiescent high viscosity parameter of  $\alpha \simeq 0.1 - 0.2$  at all disc radii if the disc flickering is caused by magnetohydrodynamic turbulence (Geertsema & Achterberg 1992). Baptista et al. (2007) investigated the changes in disc structure along two outbursts of V2051 Oph and found that (i) the disc shrinks at outburst onset, with enhanced emission along the stream trajectory close to the circularization radius, (ii) the cooling wave characterizing the outburst decline accelerates as it travels towards disc centre, and (iii) for distances lower than 120 pc the inferred disc brightness temperatures suggest that the disc is cooler than  $T_{\text{crit}2}$  everywhere, therefore excluding DIM as a viable explanation for its outbursts. The combined results of Baptista & Bortoletto (2004) and Baptista et al. (2007) are in clear contradiction with DIM predictions, making V2051 Oph an important challenge to the prevailing DIM orthodoxy.

Wojcikiewicz, Baptista & Ribeiro (2018, hereafter Paper I) modelled the ellipsoidal variations caused by the distorted mass-donor star of V2051 Oph to infer its  $JHK_s$  fluxes, deriving a spectral type of  $M(8.0 \pm 1.5)$ , an equivalent blackbody temperature of  $T_{\text{BB}} = (2700 \pm 270) K$ , and a photometric parallax distance of  $d_{\text{MS}} = (102 \pm 16)$  pc to the binary. Here we apply eclipse mapping techniques to the infrared  $JHK_s$  light curves of Paper I, after subtraction of the ellipsoidal variations caused by the mass donor star, in order to investigate the structures and the broad-band infrared spectra of

the quiescent accretion disc of V2051 Oph. This paper is organized as follows. Sect. 2 briefly describes the observations. Sect. 3 reports the data analysis and the results, which are discussed in Sect. 4 and summarized in Sect. 5.

## 2 THE OBSERVATIONS AND THE DATA

Time-series of  $JHK_s$  photometry of V2051 Oph were collected with the OSIRIS infrared imager at the 4.1 m SOAR Telescope along the night of 2013 June 20 while the star was in quiescence. The observations framed two consecutive orbital cycles in the  $K_s$  band followed by about 1.5 orbital cycles in the  $H$  and  $J$  bands each. The reader is referred to Paper I for the details of the observations, data reduction and flux calibration procedures. Although the  $JHK_s$  observations are not simultaneous, they were obtained over a short time interval in which the object remained at the same brightness level. Therefore, we are confident that the combined  $JHK_s$  surface brightness distributions (see Sect. 3.3) do represent the broad-band infrared spectra of the V2051 Oph accretion disc at that epoch.

In Paper I we modelled the ellipsoidal variation caused by the distorted mass-donor star. For the remainder of this paper, the light curves under analysis are those after subtraction of the mass-donor star contribution. These light curves were phase-folded according to the linear plus sinusoidal ephemeris of Baptista et al. (2003),

$$T_{\text{mid}} = \text{BJDD } 2443245.97745 + 0.0624278629 \times E + 20 \times 10^{-5} \cos \left[ 2\pi \left( \frac{E - 120 \times 10^3}{127 \times 10^3} \right) \right] d, \quad (1)$$

where  $T_{\text{mid}}$  is the white dwarf mid-eclipse time and  $E$  is the binary cycle. With this ephemeris the eclipses are centred at phase zero.

## 3 DATA ANALYSIS AND RESULTS

### 3.1 The GAIA distance estimate

The GAIA Data Release 2 (Gaia Collaboration 2016, 2018; Lindegren et al. 2018) yields a trigonometric parallax of  $\pi = 8.90 \pm 0.07$  mas for V2051 Oph, which translates into a distance of  $(112.3 \pm 0.9)$  pc, consistent with the photometric parallax distance estimates of Paper I at their  $1-\sigma$  limit.

Baptista et al. (2007) found that, in order to reconcile the observed disc brightness temperatures at the 2002 August outburst maximum with the critical temperatures required by DIM, V2051 Oph should be at a distance of at least 120 pc. The above trigonometric parallax distance is lower than this limit at a confidence level above the  $8-\sigma$  limit. In fact, at a distance of 112 pc even the stronger 2000 July outburst occurred at disc temperatures below those required by DIM everywhere and along the whole outburst (Baptista et al. 2007). Therefore, unless the accretion disc of V2051 Oph is optically thin during outburst – in which case the inferred B-band blackbody brightness temperatures of Baptista et al. (2007) underestimate the true disc effective temperatures (e.g., see Sect. 3.6) – the GAIA trigonometric parallax distance estimate excludes DIM as a viable mechanism to explain the outbursts of V2051 Oph.

The good agreement between the trigonometric and the

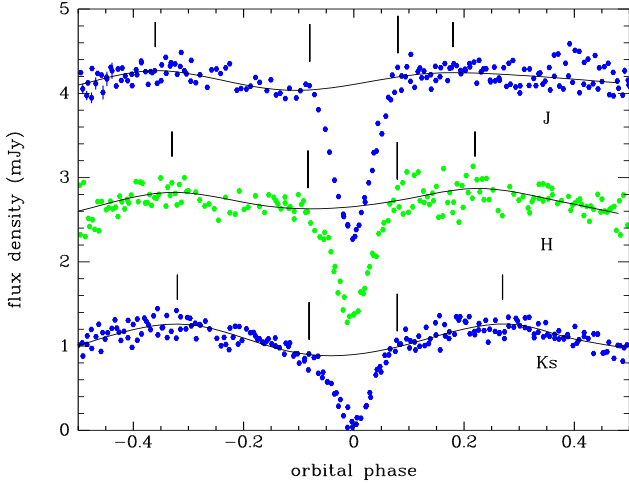


**Figure 1.** Phase-folded  $JHK_s$  light curves of V2051 Oph (dots) and the best-fit double-wave spline function to the out-of-eclipse regions (solid line). The  $J$  and  $H$  light curves are vertically displaced, respectively, by 1 and 2 mJy for visualization purposes. Small vertical ticks show the phases of maximum of the double-wave modulation; large vertical ticks mark the phases of eclipse ingress/egress.

**Table 1.** Parameters derived from the  $JHK_s$  light curves

Parameter	$J$	$H$	$K_s$
$\phi_{\max 1}$	-0.36(2)	-0.33(3)	-0.32(2)
$\phi_{\max 2}$	+0.18(3)	+0.22(3)	+0.27(1)
$\Delta f$ (mJy)	0.23(3)	0.29(1)	0.37(1)
$1/2\Delta\phi_E$	0.080(2)	0.081(2)	0.082(3)
$R_d/a$	0.26(2)	0.27(2)	0.28(2)
$R_d/R_{L1}$	0.40(2)	0.41(2)	0.42(3)

photometric parallax distance estimates indicates that the mass-donor star in V2051 Oph is indistinguishable from an isolated, main sequence star of similar mass, consistent with the conclusions of Knigge, Baraffe & Patterson (2011).

### 3.2 Analysis of the light curves

Figure 1 shows the  $JHK_s$  orbital light curves of V2051 Oph after subtraction of the ellipsoidal variation caused by its mass donor star. The light curves show a double-wave modulation (at  $P_{\text{orb}}/2$ ), the amplitude of which increases with increasing wavelength. The maxima of the modulation also move towards later phases with increasing wavelength. This modulation is asymmetric in the sense that the maxima at negative phases are stronger than those at positive phases, particularly in the  $J$  and  $K_s$  bands. Thus, we may discard an explanation in terms of possible underestimation (overestimation) of the ellipsoidal variation of the mass-donor star because this would lead to a residual double-wave modulation of equal maxima (minima) centred at phases  $\pm 0.25$ , differently from what is observed. The best-fit spline function to the out-of-eclipse fluxes are shown as solid lines in Fig. 1. Measured peak-to-peak amplitudes,  $\Delta f$ , and phases of maxima from these spline fits are collected in Table 1.

We also used the spline fits to measure the half-width

of the eclipse at each passband,  $\Delta\phi_E$ , finding the phases where the fitted spline deviates from the data by  $1\sigma$  of the local, out-of-eclipse median flux, and dividing the resulting phase range by two. We then applied the method of Sulkanen, Brasuke & Patterson (1981) to estimate the disc radius at each passband from the corresponding  $\Delta\phi_E$  value. By assuming a spherical secondary star it is possible to derive the disc radius  $R_d$  in units of the orbital separation  $a$  from the analytical expression,

$$\frac{R_d}{a} = \sin(2\pi\Delta\phi_E) \sin i - \sqrt{(R_2/a)^2 - \cos^2 i}, \quad (2)$$

where  $R_2/a$  is the radius of a sphere containing the same volume as the Roche lobe of the secondary star, given by the relation (Eggleton 1983),

$$\frac{R_2}{a} = \frac{0.49q^{2/3}}{0.6q^{2/3} + \log(1+q^{1/3})}. \quad (3)$$

where  $q = M_2/M_1$  is the binary mass ratio. Values of  $R_d/a$  are transformed to  $R_d/R_{L1}$  assuming  $R_{L1}/a = 0.66 \pm 0.01$  (Baptista et al. 1998). The resulting values are listed in Table 1 (with uncertainties given in parenthesis). Since the differences are within the uncertainties, there is no evidence that the disc radius varies with wavelength.

Previous estimates of V2051 Oph disc radius from the position of the bright spot at disc rim lead to  $R_{\text{bs}}/R_{L1} = 0.56 \pm 0.02$  in a low brightness state (Baptista et al. 1998) and  $R_{\text{bs}}/R_{L1} = 0.48 \pm 0.02$  in quiescence (Baptista & Bortoletto 2004; Baptista et al. 2007). It is not clear if the inferred smaller disc radius reflects real changes in disc structure with time (i.e., changes in mass transfer rate) or if it is a consequence of systematic differences in measuring technique.

### 3.3 Eclipse mapping

The eclipse mapping method is an indirect imaging technique which translates the information in the eclipse shape into a map of the surface brightness distribution of the occulted disc regions (Horne 1985). Because the one-dimensional data light curve do not fully constrain a two-dimensional surface brightness map, a maximum entropy procedure (e.g., Skilling 1987) is used to select, among all possible solutions, the one that maximizes the entropy of the eclipse map with respect to a smooth default map (Baptista 2001, 2016). The usual choice of default map leads to the most nearly axi-symmetric map that fits the data.

In order to improve the signal-to-noise ratio and to minimize the influence of flickering, the light curve of each passband was binned to phase resolutions of  $\delta\phi = 0.007$  and  $0.025$ , respectively during eclipse ( $\Delta\phi = -0.1, +0.1$ ) and outside of eclipse. The median flux was computed for each bin; the median of the absolute deviations with respect to the median was taken as the corresponding uncertainty at each bin. Maximum entropy eclipse mapping techniques were applied to the  $JHK_s$  binned light curves to solve for a map of the surface brightness distribution of the accretion disc and for the flux of an additional uneclipsed component in each passband.

At the high inclination of V2051 Oph, flaring of its accretion disc (at half-opening angle  $\beta$ ) may lead to perceptible differences in apparent brightness between the near and far

sides of the disc (seen at effective angles of  $i + \beta$  and  $i - \beta$ , respectively), and ignoring this effect may have a significant impact in the interpretation of eclipse mapping results. Therefore, as a first step, we used a 3D version of the eclipse mapping method in which the eclipse map is a conical surface with side  $2R_{L1}$  centred at the WD position and inclined at a half-opening angle  $\beta$  with respect to the orbital plane, plus a circular rim orthogonal to the orbital plane at a distance  $R_d$  ( $< R_{L1}$ ) from the disc centre. The disc rim radius  $R_d$  and half-opening angle  $\beta$  are additional free parameters of the method, which can be inferred from an entropy landscape procedure (Baptista, Borges & Oliveira 2016, and references therein): eclipse maps are computed for a range of  $(R_d, \beta)$  pairs of values and the resulting space of parameters is searched for the combination that yields the eclipse map of highest entropy. The resulting space of parameters is well behaved with a single, well defined entropy maximum in each case. We find  $R_d/R_{L1} = 0.42 \pm 0.05$  independent of passband, in good agreement with the disc radius estimated from the width of the eclipse. We also find  $\beta = 0.0^\circ \pm 0.5^\circ$ , indicating that the accretion disc of V2051 Oph is geometrically thin.

Given that the disc half-opening angle is negligible, we decided to proceed with a standard, 2D version of the eclipse mapping code in which the eclipse map is a flat cartesian grid of  $51 \times 51$  pixels centred at the WD position with side  $2R_{L1}$ . The eclipse geometry is defined by the mass ratio  $q$  and the binary inclination  $i$ , and the scale of the map is defined by the value of  $R_{L1}$ . We adopted  $q = 0.19 \pm 0.03$ ,  $i = 83.3^\circ \pm 1.4^\circ$  and  $R_{L1} = (0.422 \pm 0.015)R_\odot$ , which correspond to a WD eclipse width of  $\Delta\phi = 0.0662 \pm 0.0002$  (Baptista et al. 1998). This combination of parameters ensures that the WD is at the centre of the map. Because this version of the eclipse mapping method does not take into account out-of-eclipse brightness changes, these were removed by dividing each light curve by the corresponding best-fit spline function (Sect.3.2), and scaling the result to the average out-of-eclipse flux level. The resulting light curves are shown in the left-hand panels of Fig.2.

Our eclipse mapping code implements a scheme of double default functions,  $D_+D_-$ , simultaneously steering the solution towards the most nearly axi-symmetric map consistent with the data ( $D_+$ ), and away from the criss-crossed arcs along the edges of the shadow of the occulting, mass donor star ( $D_-$ ) (Spruit 1994; Baptista et al. 2005; Baptista 2016). It is optimized to recover asymmetric structures in eclipse maps such as spiral arms and enhanced gas stream emission. The positive default function is a polar Gaussian with radial and azimuthal blur widths of  $\Delta r = 0.02R_{L1}$  and  $\Delta\theta = 30^\circ$ , respectively. The negative default function is a Gaussian along the ingress/egress arcs of phase width  $\Delta\phi = 0.01$ .

The uncertainties in the eclipse maps were derived from Monte Carlo simulations with the light curves, generating a set of 50 randomized eclipse maps (see Rutten, van Paradijs & Tinbergen 1992). These are combined to produce a map of the standard deviations with respect to the true map. A map of the statistical significance (or the inverse of the relative error) is obtained by dividing the true eclipse map by the map of the standard deviations (Baptista et al. 2005). The uncertainties obtained with this procedure are used to plot the confidence level contours in the eclipse maps of Fig. 2 and to estimate the uncertainties of the spatially-resolved disc spectra (Figs. 4 and 5). The un-

certainities in the eclipse geometry (derived from the errors in the binary parameters) are negligible in comparison with the statistical uncertainties affecting the eclipse maps. An additional systematic uncertainty of 10 per cent was added in quadrature to the uncertainty of each data point in the spatially-resolved disc spectra to account for the errors introduced by the subtraction of the contribution of the mass donor star from the light curves. This has a minor effect in the results as the statistical uncertainties of the spatially-resolved spectra are dominant, in most of the cases being around the 15-20 per cent level.

### 3.4 Spiral structures in the accretion disc

Data and model light curves and corresponding eclipse maps in a logarithmic grayscale are shown in Fig. 2. The uneclipsed component corresponds to about 1, 4 and less than 1 per cent of the total flux, respectively in the  $J$ ,  $H$  and  $K_s$  bands, indicating no significant contribution from a stellar disc wind to the infrared light of V2051 Oph in quiescence. The statistical significance of the structures in the eclipse maps are at the  $3\sigma$  and above the  $5\sigma$  confidence levels, respectively for the outer (fainter) and inner (brighter) disc regions. The eclipse maps show no evidence of a bright spot at disc rim, and no enhanced emission along the gas stream trajectory.

While the  $J$  and  $K_s$  eclipse maps are dominated by emission from a central brightness source, they display asymmetries in their outer regions which suggest the presence of an elliptical outer disc with major axis roughly along the direction perpendicular to the line joining both stars (the vertical direction in Fig. 2). This is in line with the expected orientation of the two-armed spiral structure that may be induced in the outer disc regions by the tides from the mass-donor star (Sawada, Matsuda & Hachisu 1986; Boffin 2001; Steeghs 2001, and references therein). Indeed, the  $H$ -band light curve shows the characteristic 'bulge' in the eclipse shape which signals the presence of a two-armed spiral structure in an accretion disc and is reminiscent of the light curves of the eclipsing dwarf nova IP Peg in outburst (Baptista, Harlaftis & Steeghs 2000; Baptista et al. 2005). Accordingly, the corresponding eclipse map shows two clear asymmetric arcs in the outer disc regions, located in the upper left (arm 1) and lower right (arm 2) quadrants. The resemblance of the  $H$ -band light curve and eclipse map of V2051 Oph with the light curves and corresponding eclipse maps of IP Peg in outburst lead us to interpret the observed asymmetric arcs as tidally-induced spiral arms in the quiescent disc of V2051 Oph.

Two-armed spiral structure in high inclination accretion discs lead to a double-wave orbital modulation, with maxima coinciding with the binary phases where the spiral arms are seen face-on (e.g., Steeghs 2001; Baptista et al. 2005). The right-hand panels of Fig. 2 show the  $JHK_s$  eclipse maps of V2051 Oph with their central regions ( $R < 0.2R_{L1}$ ) masked for a clearer view of the asymmetries in the outer disc regions. Small red arcs indicate the azimuths of maximum emission of the double wave modulation in each case. They are in good agreement with the azimuths where the spiral arms in the eclipse maps are seen face-on. This provides additional support for the interpretation that the asymmetric arcs seen in the eclipse maps correspond to tidally-induced

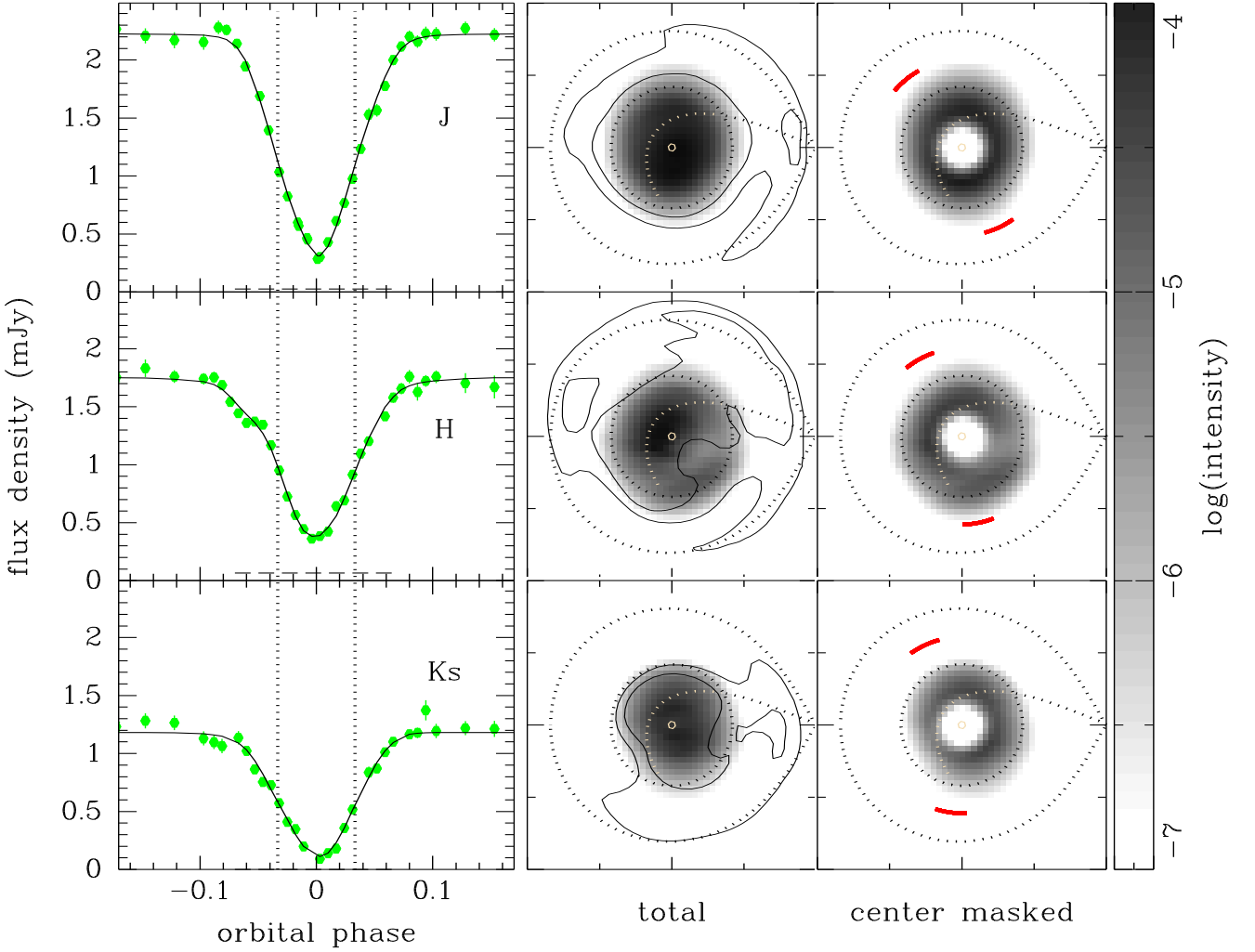


**Figure 2.** Left-hand:  $JHK_s$  data (dots with error bars) and model (solid lines) light curves. Horizontal dashed lines indicate the unocculted flux in each passband. Vertical dotted lines mark the ingress/egress phases of the WD eclipse. Middle: eclipse maps in a logarithmic grayscale. Regions inside the two solid contour lines are above the  $3\sigma$  and  $5\sigma$  confidence levels, respectively. A circle marks the position/size of the WD at disc center. Dotted lines depict the primary Roche lobe, the gas stream trajectory and a circle of radius  $0.42R_{L1}$ . Right-hand: the eclipse maps with their central regions ( $R < 0.2R_{L1}$ ) masked for a clearer view of the outer disc regions. Small arcs (red) indicate the azimuths of maximum emission of the double wave modulation in each case. The rightmost vertical bar shows the logarithmic intensity grayscale; brighter regions are darker.

spiral arms. The azimuths of maximum double wave emission rotate clockwise with increasing wavelength, suggesting that the temperature along the spiral structure decreases towards their tails (i.e., towards larger radii).

In order to investigate the properties of the asymmetric arcs we followed the steps of [Baptista, Harlaftis & Steeghs \(2000\)](#) and divided the  $H$ -band eclipse map into azimuthal slices (i.e., “slices of pizza”), computing the radius at which the intensity is a maximum for each azimuth. A corresponding Keplerian velocity is obtained for the radius of maximum intensity assuming  $M_1 = (0.78 \pm 0.06)M_\odot$  and  $R_{L1} = (0.422 \pm 0.015)R_\odot$  ([Baptista et al. 1998](#)). This exercise allows us to recover the location of the spiral structures both in radius and in azimuth (e.g., [Baptista, Harlaftis & Steeghs 2000](#); [Baptista et al. 2005](#)). Fig. 3 shows the azimuthal intensity distribution  $I_{\max}$ , corresponding radius  $R(I_{\max})$  and

Keplerian velocity  $v_{\text{kep}}[R(I_{\max})]$ . Azimuths are expressed in terms of orbital phase; these are measured from the line joining both stars and increase clockwise. The two-armed asymmetric structures in the  $H$ -band eclipse map lead to a double-humped shape in the azimuthal intensity distribution. The maxima indicate the positions of arms 1 and 2, whereas the valleys trace the region in between the spirals. The binary phases of maximum intensity of the spiral arms are in good agreement with the observed phases of maximum of the double-wave orbital modulation (indicated by horizontal tick marks in Fig. 3). Similar to IP Peg ([Baptista, Harlaftis & Steeghs 2000](#)), the spiral arms are located at different distances from disc centre. The maximum intensity along the outer arm 2 occurs at a radius of  $0.42 \pm 0.02R_{L1}$  ( $v_{\text{kep}} = 910 \pm 50 \text{ km s}^{-1}$ ), whereas that of the inner arm 1 is at  $0.28 \pm 0.02R_{L1}$  ( $v_{\text{kep}} = 1120 \pm 60 \text{ km s}^{-1}$ ).

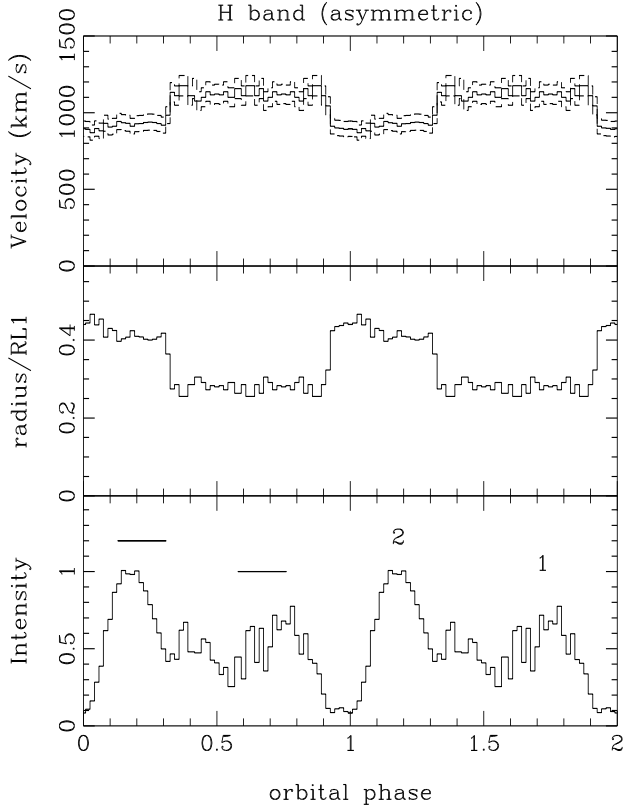


**Figure 3.** Dependency with binary phase of the maximum intensity, radius and corresponding Keplerian velocity at maximum intensity as derived from the  $H$ -band map. Intensities are plotted in an arbitrary scale; arms 1 and 2 are labeled and the phases of maxima of the double-wave orbital modulation are indicated by horizontal tick marks. Keplerian velocities were computed assuming  $M_1 = 0.78 \pm 0.02 M_\odot$  and  $R_{L1} = 0.422 \pm 0.015 R_\odot$  (Baptista et al. 1998). Dashed lines in the velocity panel shows the uncertainties at the  $1\sigma$  limit.

As a consequence of the intrinsic azimuthal smearing effect of the eclipse mapping method, spiral arms are smeared in the azimuthal direction; their trace in the azimuthal intensity distribution will always be at a constant average radius which cannot be used to estimate the opening angle of the spirals (Baptista, Harlaftis & Steeghs 2000; Harlaftis et al. 2004; Baptista et al. 2005). Instead, Baptista et al. (2005) realized that the opening angle of the spirals  $\theta_s$  can be estimated from the orientation of the valleys in the azimuthal intensity distribution, which rotate clockwise as the opening angle decreases and the spirals wind up. They found that the orbital phase of lowest intensity (the valley) in the azimuthal intensity distribution correlates to the opening angle of the spirals through the expression,

$$\theta_s(\text{degrees}) = \frac{23.25}{\phi_1(I_{\min})} - 29.6, \quad (4)$$

where  $\phi_1(I_{\min})$  corresponds to the first of the two orbital phases of intensity valleys in the azimuthal intensity distribution (if the spirals are diametrically opposed,  $\phi_1 = \phi_2 - 0.5$ ). We fitted a parabola to the intensities around the second, better defined valley of the azimuthal inten-

sity distribution of Fig. 3 and assumed diametrically opposed spiral arms<sup>2</sup> to find  $\phi_1(I_{\min}) = 0.460 \pm 0.035$ , corresponding to an opening angle of  $\theta_s = 21^\circ \pm 4^\circ$ . The opening angle inferred for the spiral arms in the quiescent disc of V2051 Oph is in between those seen in IP Peg 5-6 days ( $\theta_s = 25^\circ \pm 3^\circ$ , Baptista et al. 2005) and 8-9 days ( $\theta_s = 14^\circ \pm 3^\circ$ , Baptista, Haswell & Thomas 2002) after outburst onset.

Additional evidence for the presence of tidally-induced spiral arms in the quiescent accretion disc of V2051 Oph comes from the Doppler tomography studies of Papadaki et al. (2008), who observed V2051 Oph in quiescence two days after the end of its 1999 superoutburst, and of Rutkowski et al. (2016), who framed V2051 Oph in quiescence several months after an outburst. The trailed spectrograms of Papadaki et al. (2008) shows double peaked emission lines, the brightness and velocity separation of which are modulated at half the orbital period — a known signature of spiral arms in accretion discs (See also Sect. 3.2). Accordingly, their Balmer and He I tomograms show two asymmetric arcs extended in azimuth at opposite sides of the accretion disc, the trace of which bends towards lower velocities with increasing binary phase (as expected for a spiral pattern moving towards progressively larger radii with binary phase, see e.g. Fig. 4 of Steeghs & Stehle 1999). These arcs are reminiscent of the spiral structures seen in Doppler tomograms of IP Peg in outburst (Steeghs, Harlaftis & Horne 1997), but rotated in phase by  $\Delta\phi \sim 0.1 - 0.15$ . This apparent rotation led Papadaki et al. (2008) to discard the possible interpretation of the observed structures in terms of tidally-induced spiral arms with the argument that their orientation would be unusual. However, spiral arms observed in Doppler tomograms of outbursting dwarf novae appear at distinct orientations for different objects (see, e.g., Fig. 11 of Steeghs 2001), and the Doppler tomography of U Gem in outburst shows that the line emission from its spiral arms does rotate significantly in azimuth as the system declines from outburst maximum (Groot 2001), possibly reflecting changes in line emissivity along its spiral pattern. Interestingly, Patterson et al. (2003) performed photometric monitoring of V2051 Oph along the same 1999 superoutburst and found that, aside of the superhump signal, there were significant power at  $P_{\text{orb}}/2$ , suggesting that tidally-induced spiral arms were already present in its accretion disc during superoutburst, coexisting with the elliptical precessing disc.

Rutkowski et al. (2016) performed Doppler tomography over three consecutive orbits of V2051 Oph in quiescence, 150 days after the end of the previous outburst. Their  $H\alpha$  tomogram shows a one-armed spiral structure, while the tomograms of all other Balmer, He I and O I lines show clear two-armed spiral structures at the location where they are usually seen in outbursting dwarf novae (e.g., Steeghs 2001), which they interpreted as tidally-induced density waves. They estimated the disc temperatures from the Doppler tomograms and found no enhanced temperatures at the location of the two-armed spirals, suggesting that these structures are likely the result of increased density instead of being caused by strong hydrodynamical shocks.

<sup>2</sup> Given that the two arcs are separated in phase by  $\simeq 0.5$ , the assumption that the spiral arms are diametrically opposed seems a reasonable one.

The AAVSO database on V2051 Oph shows that the nearest recorded outburst occurred 42 days before our observations and was apparently just a normal outburst. Therefore, the interpretation of Papadaki et al. (2008) that the inner arm is related to the bright spot and the outer arm is reminiscent superhump light source is neither a plausible explanation for our observations nor for those of Rutkowski et al. (2016). On the other hand, the interpretation of the two-armed spiral structure seen in the Doppler tomograms of Papadaki et al. (2008), Rutkowski et al. (2016), and in our eclipse maps as tidally-induced spiral arms, provides a simple and plausible explanation for all observations.

### 3.5 Spatially-resolved disc spectra

Our broad-band  $JHK_s$  eclipse maps yield spatial information about the emerging infrared spectrum of the V2051 Oph accretion disc. By combining the three intensity maps we are able to recover broad-band infrared spectra at different disc locations.

We extracted disc spectra as a function of radius by dividing the maps into concentric annular regions of width  $0.05R_{L1}$  centered at the WD. The radial width of the regions is chosen based on the spatial resolution and the signal-to-noise ratio of the eclipse maps. In order to minimize the contribution of the spiral arms to the disc emission, each spectrum is obtained by computing the median intensity of all pixels inside the corresponding annulus; the standard deviation of the randomized eclipse maps (see Sect. 3.3) with respect to the median intensity is added in quadrature to the 10 per cent uncertainty from the subtraction of the contribution from the mass donor star to the light curves, and the result is taken as the corresponding uncertainty for each annulus. The resulting broad-band disc spectra are shown in Fig. 4. Ordinates are given in terms of flux per pixel in the eclipse map as seen at the Earth (a quantity independent of distance). The disc is hot and optically thin in its inner regions (with the Brackett jump clearly in emission) and becomes cold and opaque in the outer regions, those containing the spiral arms.

Given that there is yet no accepted, detailed accretion disc atmosphere model which describes how temperature changes in the vertical direction, particularly in quiescence, the following modelling of the observed disc spectra should be looked at with some reservation.

The flux per pixel in the eclipse maps,  $f_v$ , is related to the intrinsic intensity of the corresponding pixel,  $I_v$ , by the expression  $f_v = \Theta^2 I_v$ , where its solid angle is given by,

$$\Theta^2 = \left( \frac{2 R_{L1}}{N d} \right)^2 \cos i = \left( \frac{2 R_{L1}/R_{\odot}}{N d/Kpc} \right)^2 \cos i \left[ \frac{R_{\odot}}{Kpc} \right]^2, \quad (5)$$

and  $N = 51 \times 51$  is the total number of pixels in the eclipse map. Adopting  $R_{L1} = (0.422 \pm 0.015) R_{\odot}$ ,  $d = (112.3 \pm 0.9) pc$  and  $i = 83.3^\circ \pm 1.4^\circ$  leads to  $\Theta_D^2 = (2.5 \pm 0.5) \times 10^{-3} (R_{\odot}/Kpc)^2$ .

Because our broad-band infrared spectra consist of only three data points, we are bound to fitting them with spectral models of up to two free parameters. Therefore, we fixed the distance (i.e.,  $\Theta^2$ ) and used the synphot/IRAF<sup>3</sup> pack-

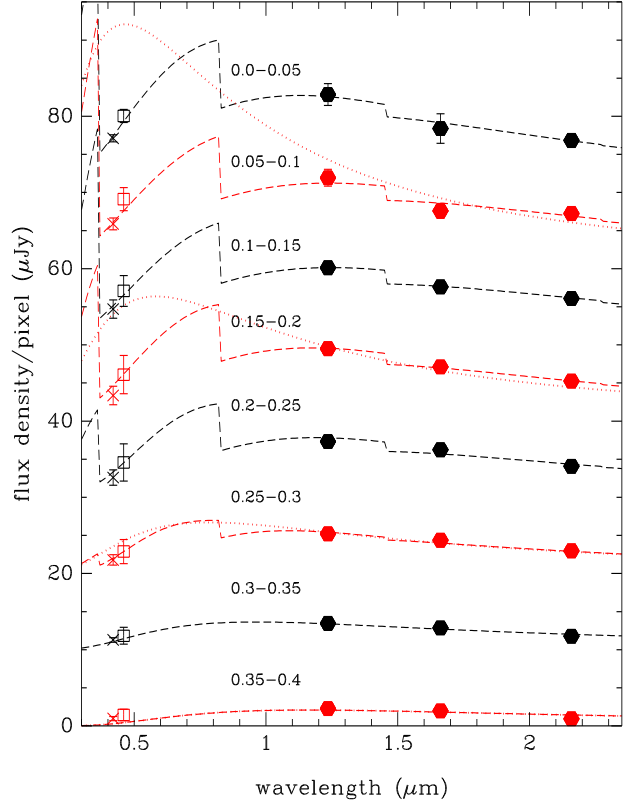


**Figure 4.** Spatially-resolved  $JHK_s$  disc spectra computed for a set of concentric annular sections (radial range indicated on the left side in units of  $R_{L1}$ ). Error bars were derived via Monte Carlo simulations with the eclipse light curves. Except for the lowest, each spectrum was vertically offset by  $10 \mu Jy$  from the previous one for visualization purposes. Dashed lines show the best-fit LTE bound-free plus free-free hydrogen continuum emission spectrum in each case, while red dotted lines show the best-fit blackbody model in four cases. The best-fit models were extrapolated to the optical range in order to allow a direct visual comparison with the observed  $B$ -band fluxes from the 'faint' (crosses) and 'bright' (open squares) quiescent states of Baptista & Bortoletto (2004). The  $B$ -band fluxes were horizontally displaced from the central wavelength of the  $B$ -band for visualization purposes ( $1 \mu Jy = 10^{-29} erg cm^{-2} s^{-1} Hz^{-1}$ ).

age to generate grids of  $JHK_s$  fluxes for blackbodies (effective temperature  $T_{ef}$  as free parameter), stellar atmosphere models ( $T_{ef}$  and  $\log g$ ), and LTE bound-free plus free-free hydrogen continuum emission spectra ( $T_{gas}$  and column density  $N(H)$ ) covering a range of input parameter values. We then computed the chi-square between the disc spectra and the fluxes in the grid of models to find the region of best-fit parameter combination in each case, and we further improved the solution using a refined grid around the best-fit region. Because of the Brackett jump in emission, blackbodies and stellar models do not provide good fits to the spectra

vatories, which are operated by the Association of Universities for Research in Astronomy, Inc., under cooperative agreement with the National Science Foundation.

<sup>3</sup> IRAF is distributed by the National Optical Astronomy Obser-

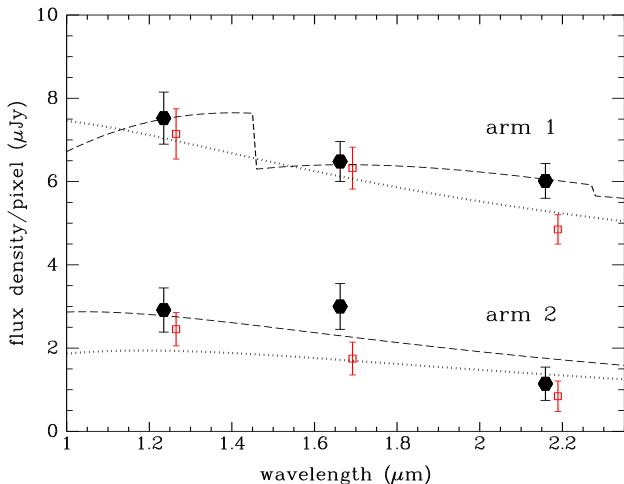


**Figure 5.** Spatially-resolved  $JHK_s$  spectra of the spiral arms (filled circles) and of the disc at the same radial range (open squares). The notation is similar to that of Fig. 4. The best-fit corresponding LTE bound-free plus free-free hydrogen continuum emission models are shown as dashed (spiral arms) and dotted (disc) lines.

of the inner disc regions ( $R < 0.3R_{L1}$ ); best-fit blackbodies and hydrogen emission models are indistinguishable in the outer, opaque disc regions ( $R \geq 0.3R_{L1}$ ). The best fit solutions ( $\chi^2_{\text{red}} \leq 1$ ) are obtained with the bound-free plus free-free hydrogen emission model in all cases; these are shown as dashed lines in Fig. 4. Uncertainties in the fitted parameters were derived from Monte Carlo simulations with the fluxes of the spatially-resolved disc spectra, subjecting the set of randomized spectra to the same fitting procedure. Quoted uncertainties are the standard deviation with respect to the average parameter value in each case.

We further tried fitting the data using blackbody spectra with  $\Theta^2$  as a second free parameter, but this results in chi-square values which are larger than and comparable to the bound-free plus free-free hydrogen emission model fit, respectively at the inner (optically thin) and outer (opaque) disc regions. Increasing the solid angle ( $\Theta^2 > \Theta_D^2$ , implying  $\cos i_{\text{ef}} > \cos i$  and larger pixel effective surface) does not improve the quality of the fits. Therefore, we found no evidence of vertically extended emission anywhere in the disc.

The inner disc atmosphere is made of hot ( $T_{\text{gas}} \sim 10 - 12 \times 10^3 \text{ K}$ ) and tenuous gas (with corresponding surface densities  $m_H N(H) \sim 10^{-3} - 10^{-2} \text{ g cm}^{-2}$ , where  $m_H$  is the hydrogen mass). The inferred surface densities are several orders of magnitude smaller than those predicted by the DIM ( $\sim 10^1 - 10^2 \text{ g cm}^{-2}$ , see e.g. Lasota 2001) and those expected for viscous, steady-state discs at low mass accretion rates ( $\sim 0.5 - 1 \text{ g cm}^{-2}$  for  $\alpha = 1$  and  $\dot{M} = 10^{-11} M_{\odot} \text{ yr}^{-1}$ , Frank, King & Raine 2002), and can only be matched by unrealistically large disc viscosities ( $\alpha > 10^4$ ) or unrealistically low mass accretion rates of  $10^{-16} - 10^{-14} M_{\odot} \text{ yr}^{-1}$ . Our results suggest that either an extended hot and tenuous chromosphere veils the emission from an underlying, colder accretion disc up to  $R \sim 0.3R_{L1}$ , or that the inner disc itself has evaporated into a hot and tenuous corona — although such quiescent accretion disc corona are expected to be much hotter than the  $\sim 10^4 \text{ K}$  inferred from our

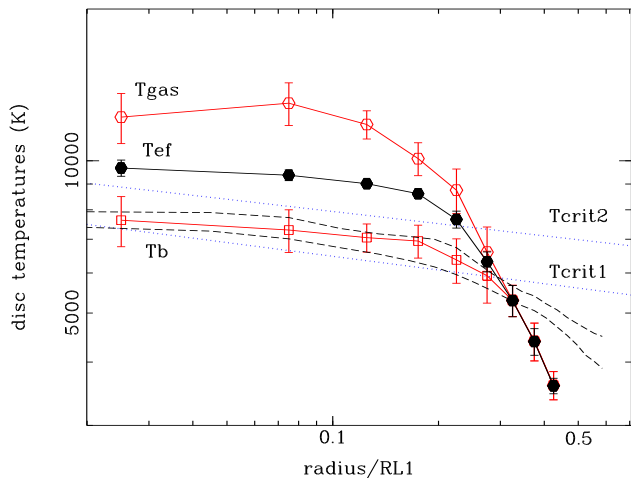
study (e.g., Meyer, Liu & Meyer-Hofmeister 2000; Hellier 2001; Barbera, Orlando & Peres 2017). These results are in good agreement with and underscore the previous findings of Vrielmann, Stiening & Offutt (2002) and Saito & Baptista (2006) — which suggested that the quiescent accretion disc of V2051 Oph is a sandwich of a cool, optically thick underlying disc with hot chromospheric layers on both sides —, and of Berriman, Kenyon & Bailey (1986), which found that most of the V2051 Oph disc would consist of hot and optically thin gas for binary distances above 100 pc (as confirmed by Paper I and the results of Sect. 3.1).

Fig. 4 shows the  $JHK_s$  best-fit models extrapolated to the optical range in order to allow a direct visual comparison with the observed  $B$ -band fluxes derived by Baptista & Bortoletto (2004) from their 'faint' (crosses) and 'bright' (open squares) V2051 Oph quiescent states. We remark that these optical observations were not included in the fitting process, as they correspond to a different epoch than that of our data. Nevertheless, the  $JHK_s$  best-fit hydrogen continuum emission models are in very good agreement with the  $B$ -band observations of Baptista & Bortoletto (2004), suggesting that the inner disc regions were also optically thin and with a similar radial temperature distribution during their observations. We note that such good agreement weakens the idea of an underlying cooler and opaque inner disc, as neglecting such a component in the spectral fit would lead to predicted  $B$ -band model fluxes which would systematically deviate from the observations. Our  $JHK_s$  best-fit hydrogen continuum emission models also predict strong Paschen and Balmer jumps in emission in the inner and intermediate disc regions, in line with the findings of Saito & Baptista (2006) — although it is worth noting that their observations correspond to the  $B \simeq 16.2$  mag unusual, low brightness state reported by Baptista et al. (1998).

Red dotted lines in Fig. 4 show the best-fit blackbody model in four cases. They largely overestimate the  $B$ -band observations of Baptista & Bortoletto (2004) in the optically thin disc regions and only provide a reasonable match to their data in the outer, optically thick disc regions where blackbodies are indistinguishable from the best-fit hydrogen continuum emission models.

We investigated the emission from the spiral arms by computing average  $JHK_s$  fluxes at annular regions of radial width  $0.1R_{L1}$  and azimuthal extent  $60^\circ$  around the position of each arm, and we also extracted comparison disc spectra at the same radial range but complementary azimuths (median fluxes, as before). The increased radial width compensates for the limited azimuthal extent and helps to preserve the signal-to-noise ratio of the spiral arms spectra. The resulting spectra are shown in Fig. 5 as solid circles (spiral arms) and open squares (disc at same radial range). The fluxes of the spiral arms are systematically larger than those of the disc at same radial range, although the differences are within the  $2\text{-}\sigma$  level. Modelling of these spectra with LTE bound-free plus free-free hydrogen continuum emission models indicate the spiral arms are hotter and have lower column densities than the disc at same radial range, but that the differences in  $T_{\text{gas}}$  and  $N(H)$  are also within the  $2\text{-}\sigma$  level. Arm 1 is well described by a model with  $T_{\text{gas}} = 7300 \pm 1100 \text{ K}$  and  $\log N(H) = 24.1 \pm 2.1$ , while arm 2 is reasonably well matched by a model with  $T_{\text{gas}} = 4900 \pm 250 \text{ K}$  and  $\log N(H) = 29.8 \pm 0.6$ . We note that for  $\log N(H) \geq 25$  the column density becomes





**Figure 6.** Radial temperature distributions derived from the spatially-resolved  $JHK_s$  disc spectra. Gas temperatures are shown as open circles, corresponding effective temperatures are shown as filled circles, while predicted B-band blackbody brightness temperatures from the same models are depicted as open squares. The dashed lines show the B-band blackbody temperatures inferred by Baptista & Bortoletto (2004). Dotted lines show the two critical temperatures which bind the thermal-viscous disc instability.

meaningless and only indicates that the gas is optically thick. The best-fit models are shown in Fig. 5 as dashed (spiral arms) and dotted (disc) lines. Blackbody fits with  $T_{\text{ef}}$  and  $\Theta^2$  as free parameters show no evidence for perceptible vertical extension of the spiral arms. The relatively low temperatures inferred for the spiral arms in the V2051 Oph quiescent accretion disc suggest they are not the result of strong hydrodynamical shocks – in line with the results of Rutkowski et al. (2016).

### 3.6 The disc radial temperature distribution

Fig. 6 shows the radial gas temperature distribution derived from the accretion disc best-fit hydrogen continuum emission models of Fig. 4 (open circles). In order to allow the comparison of the results with the  $T_{\text{crit1}}$  and  $T_{\text{crit2}}$  critical temperatures which bind the thermal-viscous disc instability, we computed the effective temperature of the best-fit model at each radius from the corresponding surface flux integrated over frequency,

$$\sigma T_{\text{ef}}^4 = \pi \int_0^\infty I_\nu d\nu. \quad (6)$$

These are shown in Fig. 6 as filled circles. We further calculated the B-band fluxes predicted by the best-fit model at each radius and computed the corresponding B-band blackbody brightness temperatures. These are shown in Fig. 6 as open squares. The optically thin inner disc regions have a relatively flat temperature distribution with  $T_{\text{ef}} \sim 9 - 10 \times 10^3 \text{ K}$ ; temperatures drop fast with increasing radius in the outer, opaque disc regions. The inferred brightness temperatures are systematically lower than the corresponding effective temperatures by as much as 20 per cent in the optically thin inner disc regions, but provide accurate estimates of  $T_{\text{ef}}$

in the outer, opaque disc regions. The brightness temperatures predicted from our models are in very good agreement with those inferred by Baptista & Bortoletto (2004) from their quiescent B-band observations of V2051 Oph (shown as dashed lines in Fig. 6, and scaled to the 112 pc distance estimate of Sect. 3.1), in line with results discussed in Sect. 3.5.1. Near the outer disc radius,  $R_d \sim 0.4 R_{L1}$ , the B-band brightness temperatures predicted by the  $JHK_s$  best-fit model decline faster with radius than those inferred from the observations of Baptista & Bortoletto (2004) reflecting the fact that the accretion disc extended to a larger radius at the epoch of their observations.

The comparison of brightness ( $T_b$ ) and effective ( $T_{\text{ef}}$ ) temperatures indicate that the former may underestimate the latter by a significant amount in optically thin disc regions. Thus, we note that if the accretion disc of V2051 Oph remains optically thin during outbursts, the inferred B-band disc brightness temperatures at outburst maximum of Baptista et al. (2007) may be similarly underestimated, which could raise the inferred  $T_b \sim 8000 \text{ K}$  up to  $T_{\text{ef}} \sim 10000 \text{ K} > T_{\text{crit2}}$ , thereby removing the discrepancy between the V2051 Oph inferred disc temperatures and the predictions of the DIM.

On the other hand, if there is no underlying cool disc, the inferred  $T_{\text{ef}}$  values well above  $T_{\text{crit2}}$  bring the inner quiescent accretion disc of V2051 Oph safely to the hot stable branch and excludes the possibility of thermal-viscous driven outbursts at these regions. This may imply in an additional discrepancy between V2051 Oph and DIM predictions, as this dwarf nova shows inside-out outbursts which seem to start near the circularization radius (Baptista et al. 2007), well within the hot, optically thin inner disc regions.

## 4 SPIRAL ARMS IN A VISCOUS, QUIESCENT ACCRETION DISC?

Numerical simulations by Sawada, Matsuda & Hachisu (1986) show that accretion discs in compact binaries are prone to the appearance of a two-armed spiral density wave at their outer regions, induced by the tides from the mass-donor star. Observational confirmation of this effect first came from Doppler tomography of emission lines of the dwarf nova IP Peg in outburst by Steeghs, Harlaftis & Horne (1997), later underscored by detection of similar spiral structures in other outbursting dwarf novae (Marsh & Schwope 2016, and references therein). The observations indicate these are wide open spiral arms with  $\theta_s \simeq 15^\circ - 30^\circ$  (e.g., Baptista et al. 2005).

In an inviscid accretion disc, the opening angle of the spiral arms is of the order of  $\tan \theta_s = c_s/v_\phi$ , where  $c_s \simeq 10(T/10^4 \text{ K})^{1/2} \text{ km s}^{-1}$  is the sound speed,  $v_\phi \simeq 10^3 \text{ km s}^{-1}$  is the disc Keplerian velocity, and  $T$  is the mid-plane disc temperature (e.g., Boffin 2001). This led Savonije, Papaloizou & Lin (1994) to predict that tidally-induced spiral arms would be tightly wound and could not be detected in the relatively cool ( $T \leq 10^5 \text{ K}$ ) and geometrically thin ( $c_s \ll v_\phi$ ) accretion discs of dwarf novae. Indeed, numerical simulations of a relatively low-viscosity  $\alpha = 0.05 - 0.1$  disc by Godon, Livio & Lubow (1998) confirmed the presence of tidally-induced spiral arms but at much smaller opening angles than observed, and that unrealistically high tempera-

tures ( $\simeq 10^6 K$ ) were required in order to reproduce the wide open spiral arms seen in the IP Peg outbursting accretion disc. Additional simulations by Stehle (1999) confirmed that low-viscosity discs ( $\alpha = 0.01$ ) lead to tightly wound spiral arms, and revealed that wide open spiral arms arise when the disc viscosity is increased ( $\alpha = 0.3$ ). The comparison of these simulations tells us that it is possible to match the wide open spiral arms obtained by the low-viscosity and extremely hot disc model of Godon, Livio & Lubow (1998) at temperatures an order of magnitude lower just by increasing the disc viscosity by a factor of 3-6 (Stehle 1999). Therefore, while increasing the disc temperatures increases the opening angle of the resulting spiral arms (e.g., Makita, Miyawaki & Matsuda 2000, and references therein), increasing the disc viscosity seems to have a similar (and seemingly stronger) effect.

The point we make here is that wide open spiral arms may be more a signature of a high viscosity disc than of a hot disc, and that a large disc viscosity might lead to detectable, wide open tidally-induced spiral density waves even when the disc is relatively cool and small. Thus, the detection of spiral arms in V2051 Oph during quiescence suggests that its quiescent accretion disc has high viscosity. This is in line with the results of Baptista & Bortoletto (2004) — which inferred a high viscosity  $\alpha \simeq 0.1 - 0.2$  for the quiescent accretion disc of V2051 Oph — and with those of Baptista et al. (2007) — which suggest that the outbursts of V2051 Oph are the result of bursts of enhanced mass transfer onto a high-viscosity accretion disc.

## 5 SUMMARY

Infrared  $JHK_s$  quiescent light curves of V2051 Oph after removal of the ellipsoidal contribution from its mass donor star show an out-of-eclipse double-wave modulation the amplitude of which increases with wavelength. Eclipse maps derived from these light curves reveal two asymmetric arcs extended in azimuth at the intermediate/outer disc regions, which are reminiscent of those seen in eclipse maps of the dwarf nova IP Peg in outburst and are similarly interpreted as tidally-induced spiral density waves in the V2051 Oph accretion disc. In agreement with this interpretation, the maxima of the double-wave modulation coincide with the binary phases where the spiral arms are seen face-on. The spiral arms are located at different distances from disc centre; the inner arm is at an average radius of  $0.28 \pm 0.02 R_{L1}$  (at a corresponding Keplerian velocity of  $v_{\text{kep}} = 1120 \pm 60 \text{ km s}^{-1}$ ), while the outer arms is at  $0.42 \pm 0.02 R_{L1}$  ( $v_{\text{kep}} = 910 \pm 50 \text{ km s}^{-1}$ ). We estimate the opening angle of these spirals to be  $\theta_s = 21^\circ \pm 4^\circ$ . The detection of wide open spiral arms in V2051 Oph during quiescence suggests that its quiescent accretion disc has high viscosity.

Broad-band  $JHK_s$  disc spectra were extracted for concentric annular disc regions. The inner disc atmosphere ( $R \leq 0.3 R_{L1}$ ) is made of hot and tenuous gas ( $T_{\text{gas}} \sim 10 - 12 \times 10^3 K$  and surface densities  $\sim 10^{-3} - 10^{-2} \text{ g cm}^{-2}$ ), suggesting that either an extended hot and tenuous chromosphere veils the emission from an underlying, colder accretion disc or that the inner disc itself has evaporated into a hot and tenuous corona. The disc gas becomes cold and opaque in its outer regions ( $R > 0.3 R_{L1}$ ). The spiral arms are hotter and have lower

column densities than the disc at same radial range, with differences within the  $2\text{-}\sigma$  confidence level. The  $JHK_s$  best-fit hydrogen continuum emission models are in very good agreement with the  $B$ -band observations of Baptista & Bortoletto (2004), suggesting that the inner disc regions were also optically thin and with a similar radial temperature distribution during their observations.

$B$ -band blackbody brightness temperatures computed from our  $JHK_s$  best-fit hydrogen continuum emission models are systematically lower than the corresponding effective temperatures by as much as 20 per cent in the optically thin inner disc regions, but provide accurate estimates of  $T_{\text{ef}}$  in the outer, opaque disc regions. If the accretion disc of V2051 Oph is optically thin at outbursts, inferred  $B$ -band disc brightness temperatures at outburst may be similarly underestimated and the disc effective temperatures could be higher than  $T_{\text{crit2}}$ , thereby removing the discrepancy between the V2051 Oph inferred disc temperatures and predictions of the DIM (Baptista et al. 2007). On the other hand, in case there is no underlying cool disc, the inferred  $T_{\text{ef}}$  values well above  $T_{\text{crit2}}$  bring the inner quiescent accretion disc of V2051 Oph safely to the hot stable branch and excludes the possibility of thermal-viscous driven outbursts at this binary.

## ACKNOWLEDGEMENTS

We thank an anonymous referee for interesting discussions which helped to improve the presentation of the results. E. W. acknowledges financial support from CAPES (Brazil) and CNPq (Brazil). In this research we have used, and acknowledge with thanks, data from the AAVSO International Database that are based on observation collected by variable star observers worldwide.

## REFERENCES

- Baptista R., 2001, in *Astromotography: Indirect Imaging Methods in Observational Astronomy*, Lecture Notes in Physics 573, eds. H. M. J. Boffin, D. Steeghs & J. Cuyper (Berlin: Springer), p. 307
- Baptista R., 2016, in *Astronomy at High Angular Resolution, Astrophysics and Space Science Library 439*, eds. H. M. J. Boffin, G. Hussain, J.P. Berger, L. Schmidtobreick (Springer-Verlag: Berlin), p. 155
- Baptista R., Harlaftis E. T., Steeghs D., 2000, *MNRAS*, 314, 727
- Baptista R., Hasswell C. A., Thomas G., 2002, *MNRAS*, 334, 198
- Baptista R., Borges B.W., Bond H.E., Jablonski F., Steiner J.E., Grauer A.D., 2003, *MNRAS*, 345, 889
- Baptista R., Borges B. W., Oliveira A. S., 2016, *MNRAS*, 463, 3799
- Baptista R., Bortoletto A., 2004, *AJ*, 128, 411
- Baptista R., Catalan M.S., Horne K., Zilli D., 1998, *MNRAS*, 300, 233
- Baptista R., Morales-Rueda L., Harlaftis E. T., Marsh T. R., & Steeghs D., 2005, *A&A*, 444, 201
- Baptista R., Santos R.F., Faúndez-Abans M., Bortoletto A., 2007, *AJ*, 867
- Barbera E., Orlando S., Peres G., 2017, *A&A*, 600, 105B
- Bath G.T., Pringle J.E., 1981, *MNRAS*, 194, 967
- Berriman G., Kenyon S., Bailey J., 1986, *MNRAS*, 222, 871
- Boffin H. M. J., 2001, in *Astromotography: Indirect Imaging Methods in Observational Astronomy*, Lecture Notes in

- Physics 573, eds. H. M. J. Boffin, D. Steeghs & J. Cuypers (Berlin: Springer), p. 69
- Cook M.C., Brunt C.C., 1983, MNRAS, 205, 465
- Eggleton P. P., 1983, ApJ, 268, 368
- Frank J., King A., & Raine D., 2002, *Accretion Power in Astrophysics - 3rd. edition*, (Cambridge: Cambridge Univ. Press)
- Gaia Collaboration, Prusti T., de Bruijne J. H. J. et al., 2016, A&A, 595, A1
- Gaia Collaboration, Brown A. G. A., Vallenari A. et al., 2018, A&A, 616, A1
- Geertsema G. T. & Achterberg A., 1992, A&A, 255, 427
- Godon P., Livio M., Lubow S., 1994, MNRAS, 295, L11
- Groot P. J., 2001, ApJ, 551, L89
- Harlaftis E. T., Baptista R., Morales-Rueda L., Marsh T. R., Steeghs D., 2004, A&A, 417, 1063
- Hellier C., 2001, *Cataclysmic Variable Stars: How and why they vary* (Chichester: Springer-Praxis)
- Hirose M., & Osaki Y., 1990, PASJ, 42, 135
- Horne K., 1985, MNRAS, 213, 129
- Kiyota S., Kato T., 1998, IBVS 4644, 1
- Knigge C., Baraffe I., Patterson J., 2011, ApJS, 194, 28
- Lasota J.P., 2001, NewAR, 45, 449
- Lindegren L., Hernández J., Bombrun A. et al., 2018, A&A, 616, A2
- Lubow S. H., 1994, ApJ, 432, 224
- Marsh T. R., Schwope A. D., 2016, in *Astronomy at High Angular Resolution, Astrophysics and Space Science Library 439*, eds. H. M. J. Boffin, G. Hussain, J.P. Berger, L. Schmidtobreick (Springer-Verlag: Berlin), p. 195
- Makita M., Miyawaki K., Matsuda, T., 2000, MNRAS, 316, 906
- Meyer F., Liu B. F., Meyer-Hofmeister E., 2000, A&A, 361, 175
- Papadaki C., Boffin H. M. J., Steeghs D., Schmidtobreick, L., 2008, A&A, 487, 611P
- Patterson J., et al., 2003, PASP, 115, 1308
- Rutkowski A., Waniak W., Preston G., Pych W., 2016, MNRAS, 463, 3290
- Rutten R. G. M., van Paradijs J. & Tinbergen J., 1992, A&A, 260, 213
- Saito R. K., Baptista R., 2006, ApJ, 131, 2185
- Sanduleak N., 1972, IBVS, 663, 1
- Savonije G. J., Papaloizou J. C. B., Lin D. N. C., 1994, MNRAS, 268, 13
- Sawada K., Matsuda T., & Hachisu I., 1986, MNRAS, 219, 75
- Shakura N. I. & Sunyaev R. A., 1973, A&A, 24, 337
- Skilling J., 1987, In: *Maximum Entropy and Bayesian Methods in Applied Statistics*, ed. J. H. Justice (Cambridge University Press, Cambridge), 156
- Spruit H. C., 1994, A&A, 289, 441
- Steeghs D., 2001, in *Astrotomography: Indirect Imaging Methods in Observational Astronomy, Lecture Notes in Physics 573*, eds. H. M. J. Boffin, D. Steeghs & J. Cuypers (Berlin: Springer), p. 45
- Steeghs D., Harlaftis E. H., Horne K., 1997, MNRAS, 290, L28
- Steeghs D., Stehle R., 1999, MNRAS, 307, 99
- Stehle R., 1999, MNRAS, 304, 687
- Sulkanen M. E., Brasuke L. W. & Patterson J., 1981. ApJ, 244, 579
- Vrielmann S., Stiening R. F., Offutt W., 2002, MNRAS, 334, 608
- Vrielmann S., Offutt W., 2003, MNRAS, 338, 165
- Warner B., Cropper M., 1983, MNRAS, 203, 909
- Warner B., 1995, *Cataclysmic Variable Stars* (Cambridge: Cambridge University Press)
- Warner B., O'Donoghue D., 1987, MNRAS, 224, 733
- Whitehurst R., 1988, MNRAS, 232, 35
- Wojcikiewicz E., Baptista R., Ribeiro T., 2018, MNRAS, 475, 2675 (Paper I)

This paper has been typeset from a  $\text{\TeX}/\text{\LaTeX}$  file prepared by the author.